Micron 146 (2021) 103071

Contents lists available at ScienceDirect

Micron

journal homepage: www.elsevier.com/locate/micron

3D electron diffraction of mono- and few-layer MoS_2

Tatiana E. Gorelik *, Berkin Nergis [1], Tobias Schöner [2], Janis Köster, Ute Kaiser

Electron Microscopy of Materials Science (EMMS), Central Facility for Electron Microscopy, Ulm University, Albert Einstein Allee 11, 89081, Ulm, Germany

ARTICLE INFO

Keywords:
2D crystals
3D electron diffraction
MoS_2

ABSTRACT

Mono- and few-layer MoS_2 were studied by three-dimensional electron diffraction (3D ED) showing distinctly different symmetry for crystals consisting of odd and even number of layers. Experimentally obtained intensity distributions along the relrods match qualitatively kinematically simulated data. Our findings allow to differentiate unambiguously between 1-, 2-, 3- 4- and 5-layers MoS_2 crystals.

1. Introduction

With the discovery of the semimetal behaviour in graphene (Novoselov et al., 2004), the quest for new 2D crystals started and many exceptional physical properties were discovered (Xu et al., 2013). A successful strategy was to scan 3D crystals with similar structural features as graphite – layered materials with strong (often covalent) bonds within the layers and weak van-der-Waals forces between them (Lv et al., 2015). A significant number of new 2D materials was fabricated in the last years, featuring close graphene relatives as BN (Song et al., 2010) and BP (Liu et al., 2014), transition metal di-chalcogenides - TMDs (Choi et al., 2017) and MXenes (Gogotsi and Anasori, 2019). Due to the weak interlayer interaction, single layers could be exfoliated from the parent solids, either using the mechanical scotch-tape technique, or chemical exfoliation through the formation of an intermediate intercalated structure (Xu et al., 2013). In many cases, 2D materials could also be prepared using the bottom up strategy, e. g. CVD, topochemical synthesis, and specialized wet synthetic protocols (Zavabeti et al., 2020).

A variety of unprecedented physical properties originating from quantum confinement and surface effects were demonstrated for 2D crystals (Xia et al., 2014; Nerl et al., 2017). As an example, some bulk semiconducting TMDs with the trigonal prismatic metal coordination have an indirect band gap, while their corresponding monolayers show direct electronic and optical band gaps with enhanced photoluminescence at visible frequencies (Mak et al., 2010; Ugeda et al., 2014), making them emerging materials for nanoelectronics based on photovoltaic and photoemission (Lv et al., 2015; Xia et al., 2014; Wang et al., 2015; Choi et al., 2017).

For most TMDs, including MoS_2, different topologies of a monolayer are possible (Lv et al., 2015): (1) the trigonal prismatic coordination of the metal, forming the 2H bulk structure (H stands for hexagonal), (2) the octahedral (trigonal antiprism) coordination of the metal, forming the 1 T bulk structure (T stands for trigonal), and (3) the distorted octahedral coordination of the metal resulting in the 1 T' bulk phase (Choi et al., 2017).

The 2H bulk crystal structure is centrosymmetric, the unit cell contains 2 layers, shifted with respect to each other by 1/3 of the (a, b) cell diagonal (Fig. 1). A monolayer with the trigonal prismatic geometry does not have an inversion centre. Due to the relative layers shift, a bilayer crystal is, in contrast, centrosymmetric. Thus, crystals with odd and even number of layers possess different symmetry, and consequently their physical properties differ accordingly. For example, second harmonic generation (SHG) was reported for crystals with an odd layer number (Yin et al., 2014), while in crystals with an even layer number, no SHG was observed.

Intrigued by the symmetry switching with the increase of the layer numbers, we decided to look deeper into the crystallographic symmetry 2D TMDs. Triggered by the last developments in 3D electron diffraction (ED) methods (Gemmi et al., 2019) and their achievements in structure analysis of diverse material classes, we collected and analysed 3D ED data of mono- and few-layer 2H MoS_2. We especially were interested in the prospects of discriminating between 2H MoS_2 with different number of layers from ED data, recently demonstrated for graphene (Sung et al., 2019).

* Corresponding author.
E-mail address: tatiana.gorelik@uni-ulm.de (T.E. Gorelik).
[1] Now at: Institute for Photon Science and Synchrotron Radiation, Karlsruhe Institute of Technology, Hermann-von-Helmholtz-Platz 1, D-76344 Eggenstein-Leopoldshafen, Germany.
[2] Now at: Technical University München, Arcisstraße 21, 80333 München, Germany.

https://doi.org/10.1016/j.micron.2021.103071
Received 22 March 2021; Received in revised form 13 April 2021; Accepted 13 April 2021
Available online 15 April 2021

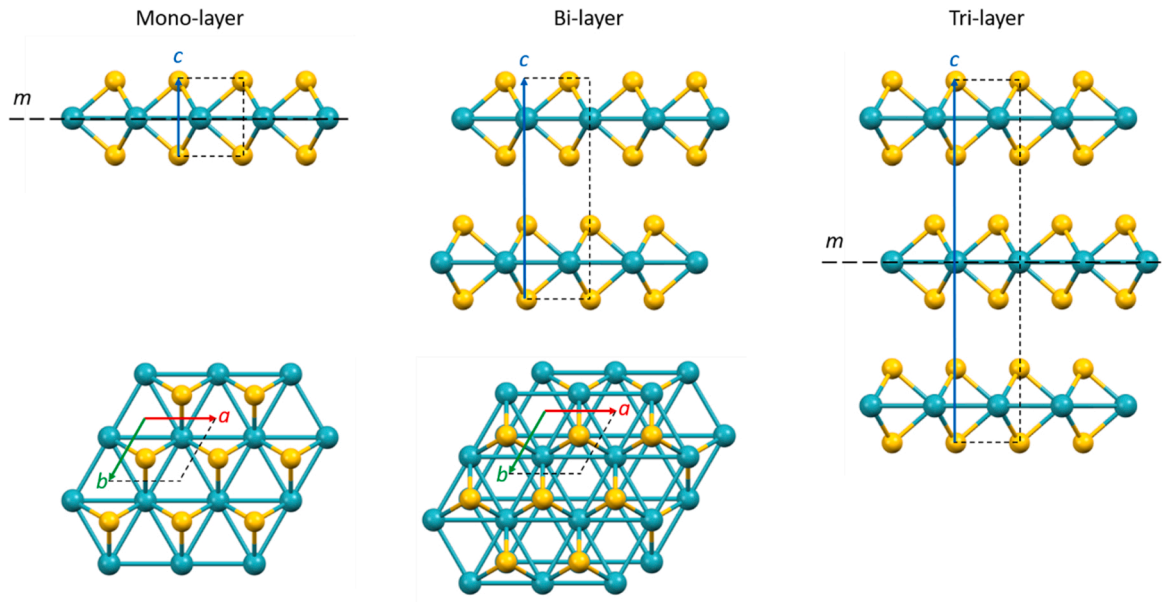

Fig. 1. Crystal structures (side and top views) of mono-, bi-, and tri-layer MoS_2 demonstrating the alternating change in the crystal symmetriey with increase of the number of layers.

2. Material and methods

Monolayer and few-layer 2H MoS_2 were prepared by mechanical exfoliation, using the scotch-tape procedure (Novoselov et al., 2004; Das et al., 2015). Flakes were mechanically exfoliated from bulk MoS_2 obtained from HQ Graphene (Groningen, Netherlands). Exfoliated flakes were transferred onto Si/SiO_2 90 nm wafer. The flake's thickness was determined by optical contrast measurements using an Olympus BX51 optical microscope and compared to the published values (Li et al., 2013). The optical image containing the selected crystals and the details for the thickness determination are presented in *Appendix A*. The selected flakes (two monolayer crystals, two bilayers, two 3-layers, and two 4-layer crystals) were attached to an Au quantifoil TEM grid using isopropanol. After the evaporation of isopropanol, SiO_2 was etched off with KOH (Lehnert et al., 2017). Grids were washed with deionized water to remove residual contamination.

Electron diffraction (ED) data were collected using a Thermofisher TITAN TEM operated at 300 kV. ED was performed in nano-diffraction geometry with a 50 μm C2 condenser aperture and an effective beam diameter on the sample of 1 μm. 3D ED tilt series were collected using a self-written Digital Micrograph (GATAN, Pleasanton, USA) script, sequentially tilting the TEM stage in a regular step and saving the recorded images. The script is provided in the Appendix B. Fischione advanced tomography holder was used for data collection. Diffraction patterns were collected within the tilt range of ±60°, stepwise, with a tilt increment of 1°.

ED tilt series were processed using EDT Process software (AnaliteX, Stockholm, Sweden) supported by self-written MatLab (The MathWorks, Inc., Natick, Massachusetts, USA) scripts. Stacks of electron diffraction patterns were centred, rotated to ensure that the tilt axis runs vertical, and intensities of reflections along the relrods (z-direction) were extracted within a small integration box.

ED data were simulated using eMap (AnaliteX, Stockholm, Sweden). A standard crystallographic program, developed to handle 3D crystals, is not able to handle confined crystals and calculate a continuously distributed intensity. In order to overcome this problem, pseudo periodic artificial crystal structures with unit cell dimensions of a = 3.15 Å, b = 3.15 Å, c = 1000 Å, γ = 120°, containing 1, 2, 3, 4 and 5 layers were created from the bulk structure. For these 5 structures, 3D Bragg reflection data were calculated. A finely spaced L index with an increment of 1/c reciprocal distance was used as an approximation for the continuous L coordinate.

Visualization of 3D ED data was made using UCSF Chimera package (Pettersen et al., 2004).

3. Results and discussion

3.1. On the symmetry of mono- and few-layer MoS_2

The bulk structure of 2H-MoS_2 has been known almost for a century. The material crystallizes in $P6_3/mmc$ (No. 194) space group with lattice parameters a = b = 3.15(2) Å and c = 12.30(7) Å (Dickinson and Pauling, 1923). The molybdenum atoms occupy the 2c (1/3, 2/3, 1/4) positions and the sulphur atoms occupy the 4f (1/3, 2/3, z) positions. The unit cell contains two alternating layers with an AB stacking along the c axis. The single layer of 2H MoS_2 is composed of a hexagonal plane of molybdenum atoms sandwiched between two hexagonal planes of the sulphur atoms (see Fig. 1). Each molybdenum atom is surrounded by six sulphur atoms in a trigonal prismatic coordination.

The symmetry of a single layer can be described by a layer group – a 3D space group including 2D translations only (Kopský and Litvin, 2002). Beside the 2D translations, a monolayer of 2H MoS_2 possesses, a vertical $\bar{6}$ axis passing through two sulphur atoms and a mirror plane running through the middle of the layer (Fig. 1). The layer group of a monolayer MoS_2 is then $p\ \bar{6}\ m2$ (No. 78), with molybdenum atoms occupying 1c (2/3, 1/3, 0) positions and sulphur atoms at 2e (1/3, 2/3, z) positions.

The Laue class represents the point symmetry of its 3D diffraction pattern, in other words, the symmetry of the reciprocal lattice weighted with the intensities of the Bragg peaks. For a MoS_2 monolayer the Laue class is *6/mmm*.

The situation is different for a bilayer. Due to the layers shift (AB stacking), the mirror plane in the middle of the structure is lost and the $\bar{6}$ axis transforms to a $\bar{3}$. The remaining symmetry elements form the layer group $p\ \bar{3}\ m1$ (No. 72), containing only vertically oriented mirror planes. Molybdenum atoms occupy 2c positions (1/3, 2/3, z), sulphur atoms are located at 2b (0, 0, z) and 2c positions. The Laue class of this group is $\bar{3}\ m1$.

3-layer MoS_2 will regain the mirror plane orthogonal to the $\bar{6}$ axis, the layer group again being $p\ \bar{6}\ m2$. Obviously, in the four-layer crystal,

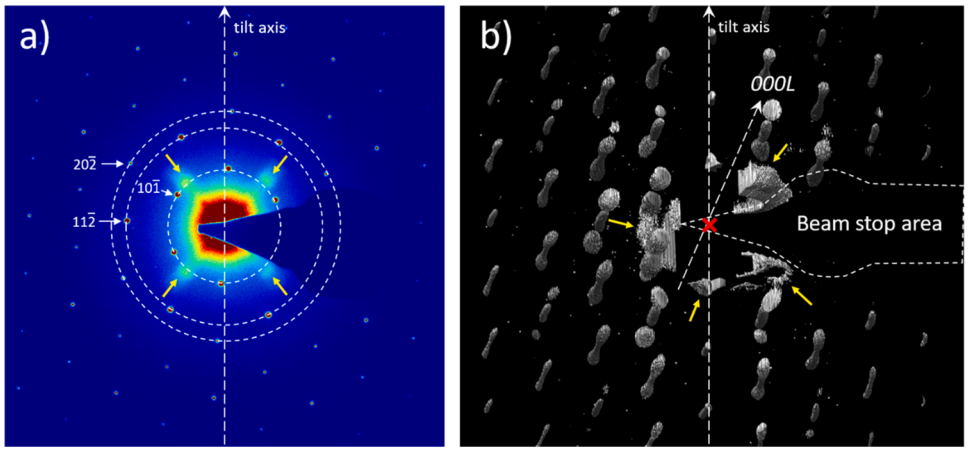

Fig. 2. (a) Experimental normal incidence electron diffraction pattern of a monolayer MoS_2, symmetry equivalent reflections are marked by dashed rings, artefacts due to the shadow of the gun tip are denoted by yellow arrows; (b) projection of the reconstruction electron diffraction space of a monolayer MoS_2 viewed along an arbitrary direction (b). Area with missing intensity in the middle of the reciprocal volume (b) appears due to the beam stop, the position of the primary beam is marked by a red cross, artefacts due to the gun shadow are reconstructed into irregular objects marked by yellow arrows.

the mirror plane will vanish again, resulting in the reduced symmetry $p\,\bar{3}\,m1$. Thus, with increasing number of layers, the symmetry of the multilayer crystal will alternate, each stack with an odd number of layers (n = 1, 3, 5, …) has a layer group symmetry $p\,\bar{6}\,m2$ (No. 78), and with an even number - $p\,\bar{3}\,m1$ (No. 72).

From these symmetry considerations it follows immediately that the 3D diffraction space must appear significantly different for crystals with odd and even layer number. The Laue class *6/mmm*, (in Schoenflies notation: D_{6h}) has a horizontal mirror plane. As a result, a crystal with an odd number of layers must produce a symmetric diffraction intensity distribution along c^* relative to the $L = 0$ position. The Laue class $\bar{3}\,m1$ does not have a horizontal mirror plane, thus a crystal with an even number of layers will have an asymmetric intensity distribution along the c^* direction, except for the *000 L* row, being symmetric due to Friedel's law.

3.2. Relrods

The size and shape of a reflection in reciprocal space is related to the size and shape of the sample in direct space. A bulk (3D) crystal produces discrete Bragg reflections at the positions determined by the basis vectors of the crystalline lattice, which are indexed by Miller indices. With the decrease of one dimension, the crystal's Bragg reflections elongate and in the extreme case of a 2D crystal, they merge and appear as continuous relrods (Fig. 2b). The corresponding Miller index running in reciprocal space along the rod, becomes a continuous coordinate *L*.

In the geometry with a parallel electron beam falling onto a 2D crystal, the zero-tilt electron diffraction pattern will represent the normal incidence zone axis pattern, for a bulk crystal corresponding to the zero-order Laue zone (ZOLZ). All tilted diffraction patterns comprise intersections of relrods with the Ewald sphere at a different height,

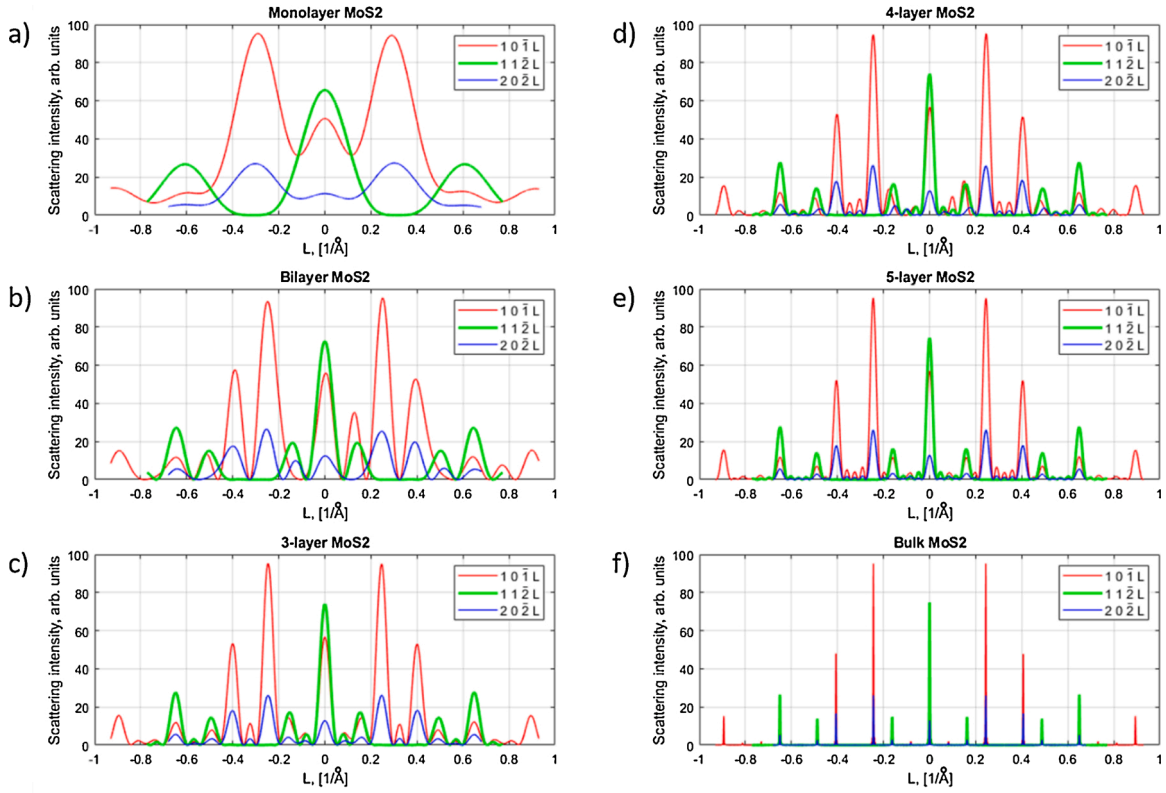

Fig. 3. Simulated intensity distribution along the relrods: a) MoS_2 monolayer, b) bilayer, c) 3-layer, d) 4-layer, e) 5-layer, and f) bulk MoS_2. Vertical scale – arbitrary units.

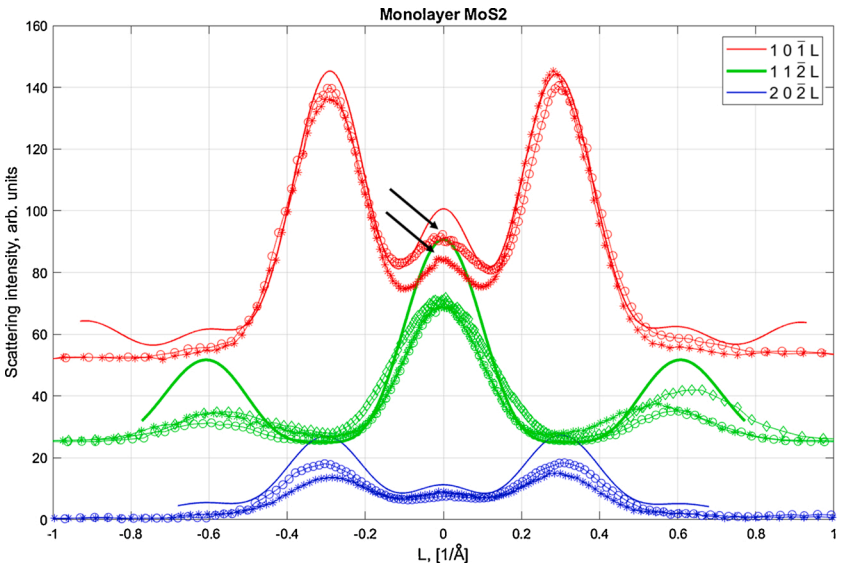

Fig. 4. Experimental (scatter plot) and simulated (solid line) scattering intensity distribution profiles along the 10 $\bar{1}$ L (red), 11 $\bar{2}$ L (green), and 20 $\bar{2}$ L (blue) relrods for a monolayer MoS_2.

depending on the tilting angle.

Bulk hexagonal structures are described using the 4 indices Miller-Bravais notation *hkil* with $h + k+i = 0$. For a 2D hexagonal lattice, analogous to the Miller-Bravais notation, we are going to use 3-indices in the form *hki* with $h + k+i = 0$, allowing for their cyclic permutation. We will use the capital *L* here for the continuous index along the relrods, to underline the differences to the discrete Miller index *l*.

For the case of a hexagonal 2H MoS_2 monolayer, the normal incidence zone axis pattern corresponds to the [0001] zone of the bulk structure and has a *p6mm* symmetry (Fig. 2a). All reflections with the same distance from the central beam are crystallographic equivalent, e.g. the set: 10 $\bar{1}$, 01 $\bar{1}$, $\bar{1}$ 10, $\bar{1}$ 01, 0 $\bar{1}$ 1, 1 $\bar{1}$ 0. For the sake of simplicity, we use "10 $\bar{1}$" notation for the whole set, and the corresponding relrods running through these reflections are denoted as *10* $\bar{1}$ *L*. Following this logic, three different types of relrods were assigned and subsequently analysed in this study – *10* $\bar{1}$ *L*, *11* $\bar{2}$ *L*, and *20* $\bar{2}$ *L* (Fig. 2b). The *000 L* rod, passing through the central spot is physically not accessible due to the limited tilt range of the goniometer.

The central point of the rod with the $L = 0$ we define as a rod *base*. The horizontal coordinate of the base is given by the in-plane interplanar distances of the structure and can easily be related to the bulk structure.

Fig. 2b shows an arbitrary projection of the reciprocal space reconstructed from a tilt series of electron diffraction patterns. The elongated relrods, appearing instead of discrete Bragg peaks are evident. The scattering intensity distribution along the relrods is very complex, being a consequence of the 3-atom (S-Mo-S) structure of a monolayer in *z* direction.

3.3. Simulated intensity distribution along the relrods

Several approximations were done in order to simulate the 3D ED data: (*i*) the atomic models were created from the bulk 2H MoS_2 structure, assuming that in 2D crystals, the atomic geometry follows the idealised 3D lattice; (*ii*) 2D crystals were approximated by a pseudo periodic 3D lattice with a large distance between the layers (~1000 Å); (*iii*) all diffraction data were simulated in kinematical approximation. Finally, no instrumental transfer function in the diffraction space (Gorelik et al., 2019) was used.

Kinematically simulated intensity distribution for 2H MoS_2 crystals with different numbers of layers is presented in Fig. 3. The data for relrods of the *10* $\bar{1}$ *L* type are shown in red, *11* $\bar{2}$ *L* – in green, *20* $\bar{2}$ *L* in blue. For comparison, Bragg reflection intensities for a bulk structure are shown in Fig. 3f; here, a peak broadening corresponding to an arbitrary crystal thickness of 30 nm (composed of 50 individual layers) was applied. All relrods contain a peak at the position of $L = 0$, for the bulk structure corresponding to 10 $\bar{1}$ 0, 11 $\bar{2}$ 0, and 20 $\bar{2}$ 0 reflections, respectively.

As expected from the symmetry of the monolayer (discussed above), a symmetric intensity distribution along *L* in respect to rod's base ($L = 0$) with broad peaks is produced (Fig. 3a). The strongest peak in the *10* $\bar{1}$ *L* rod appears at the position of 0.315 $Å^{-1}$, corresponding to the distance between the top and bottom sulphur atoms planes.

For the bilayer, an evidently asymmetric distribution in respect to the base is produced (Fig. 3b). The asymmetry is especially pronounced for the strongest *10* $\bar{1}$ *L* rod: a shoulder appears at the position of 0.162 $Å^{-1}$, absent on the left-hand side. The direct space distance corresponding to this peak is 6.15 Å, matching the distance between the molybdenum planes, being essentially the average distance between the MoS_2 layers. The central peak of the *10* $\bar{1}$ *L* rod also appears slightly shifted to the positive *L*, resulting in a slight asymmetry of the relrod at very small *L*. All peaks are significantly narrower compared to those of the monolayer.

For a 3-layer, the relrods are symmetric in respect to the base (Laue class *6/mmm*). The first weak peak at 0.081 $Å^{-1}$ corresponds to the double distance between two molybdenum layers and represents in direct space the bulk lattice parameter c. It is preserved for higher number of layers, and transforms later into the 10 $\bar{1}$ 1 Bragg peak of the bulk structure (Fig. 3f).

The 4-layer crystal shows again asymmetric relrods in respect to their base and the 5-layer crystal - symmetric. The intensities of the asymmetric peaks are relatively low, yet significant. The positions of the peaks and their intensities start resembling the bulk data shown in Fig. 3f.

3.4. Experimental intensity distribution along the relrods

3.4.1. Monolayer MoS_2

The number of layers in studied crystals was initially assigned using the optical contrast measurements (see *Appendix A*). For a monolayer, experimentally obtained and simulated intensity distribution plots along the *10* $\bar{1}$ *L*, *11* $\bar{2}$ *L* and *20* $\bar{2}$ *L* relrods are shown in Fig. 4. Two neighbouring relrods of the *10* $\bar{1}$ type could be extrated from the 3D ED data,

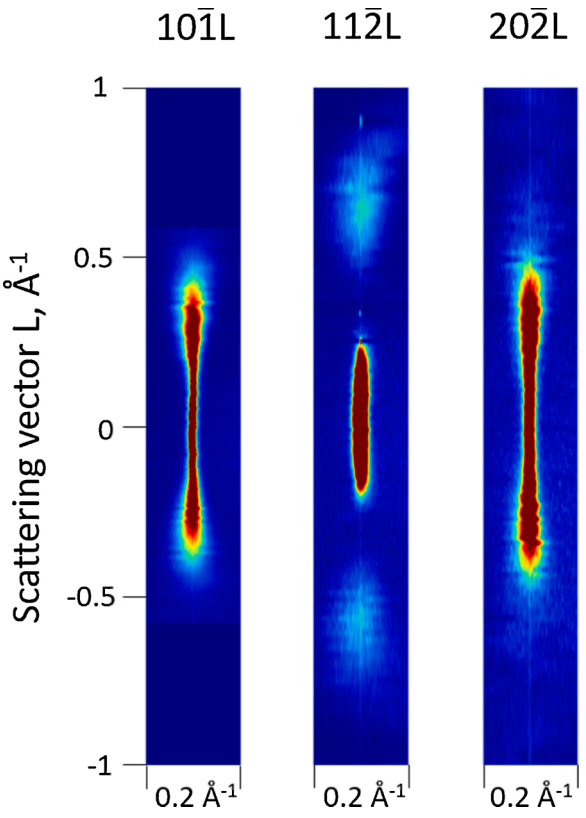

Fig. 5. Cuts of the 3D ED data showing the shape of the relrods for monolayer MoS_2.

the corresponding plots are shown as red circle and star scatter plots; three neighbouring rods of *11* $\bar{2}$ type are shown as green circle, star and diamond scatter plots, and two *20* $\bar{2}$ type rods (see Fig. 2a) are shown as blue circle and star scatter plots. The red and green plots are offset up for clarity.

Experimental plots for the same types of rods (shown in the same colour – red, green, blue) show essentially the same intensity distribution (three green plots can hardly be distinguished). The simulated intensity distribution is shown as solid lines. As can be seen from the comparison between simulated and experimental intensity distribution, apart from deviations in the middle of the *10* $\bar{1}$ *L* rods, the overal intensity distribution is described very well by the simulation.

All diffraction simulations presented in this paper were done using the kinematical formalism. Yet, it is known that the normal incidence electron diffraction pattern of a monolayer MoS_2 shows systematic violation of the Friedel law, with the difference in the intensities of 10–20 % (Brivio et al., 2011). Recently, strong phase object approximation was applied to explain this effect (Deb et al., 2020). The anomalous difference in the intensities of the Friedel mates appears for non-centrosymmetric 2D crystals containing heavy atoms, therefore can be seen as an analogue to well-known anomalous scattering in X-rays (Cromer and Liberman, 1970).

A strong deviation of intensities associated with the Friedel pairs violation is seen in the middle of the *10* $\bar{1}$ *L* rods (marked with black arrows in Fig. 4). One can see that the Friedel-mates intensity disagreement in neighbouring *10* $\bar{1}$ *L* rods at $L = 0$ is about 20 %. Noticeably, this effect is mostly pronounced for the *10* $\bar{1}$ type rods, and only at $L = 0$, i.e. within the normal incidence zone pattern. We also noticed a slight disagreement in the left and right peaks at $L = 0.3$ Å^{-1}. Whether this effect is also associated with the anomalous scattering or is a measurement artefact will be investigated in due course.

Noticeably, the widths of the peaks also match the simulated plots quite well, meaning that the main contribution to the peak width comes from the shape of the atomic scattering factors of the individual atoms.

Just as graphene (Meyer et al., 2007a, 2007b; Kirilenko et al., 2011), monolayer MoS_2 was shown to be affected by out-of-plane corrugation (Brivio et al., 2011). In the reciprocal space the corrugation manifests in the effective broadening of relrods at higher values of *L*. The broadening can be quantified and characterized by a set of corrugation waves with different amplitudes and wavelengths. For MoS_2, a rather complex intensity distribution along the relrods is overlaid with the waviness-induced broadening, so that the cuts of the relrods have a very complex shape (see Fig. 5). It may come that a proper quantification of the corrugation will need a more sophisticated formalism than that presented in (Brivio et al., 2011). In this study we did not attempt to quantify the broadening of the relrods and associated waviness parameters.

3.4.2. *Bilayer MoS_2*

Experimentally determined and simulated intensity distribution

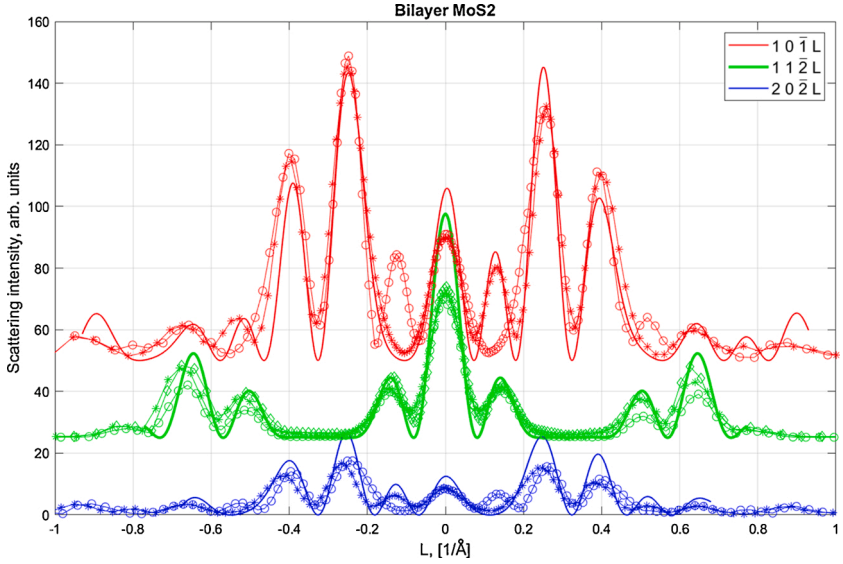

Fig. 6. Experimental (scatter plot) and simulated (solid line) scattering intensity distribution profiles along the 10 $\bar{1}$ L (red), 11 $\bar{2}$ L (green), and 20 $\bar{2}$ L (blue) relrods for a bilayer MoS_2.

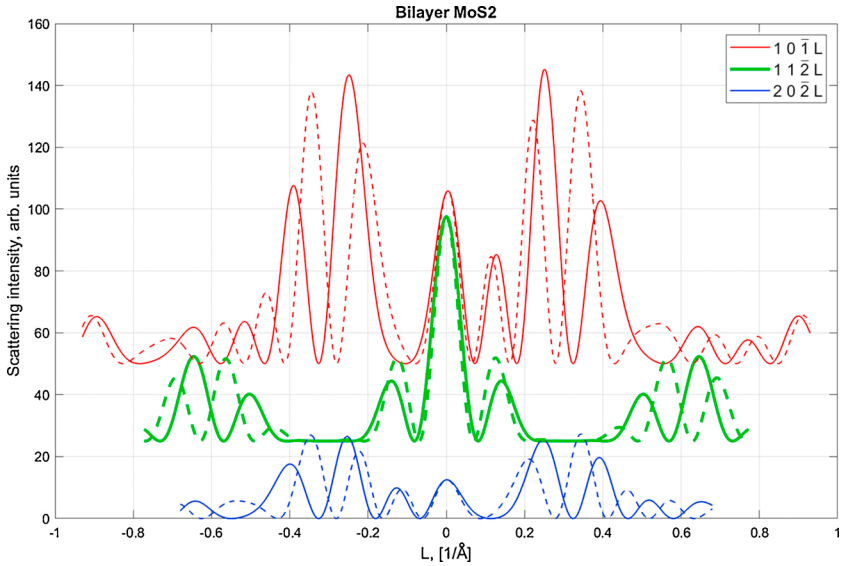

Fig. 7. Simulated scattering intensity distribution profiles along the 10 $\bar{1}$ L (red), 110 $\bar{2}$ L (green) and 20 $\bar{2}$ L (blue) relrods for a bilayer MoS_2 with the typical distance of 6.15 Å (Dickinson and Pauling, 1923) between the molybdenum planes (solid lines) and with an artificially increased distance of 7.15 Å (dashed lines).

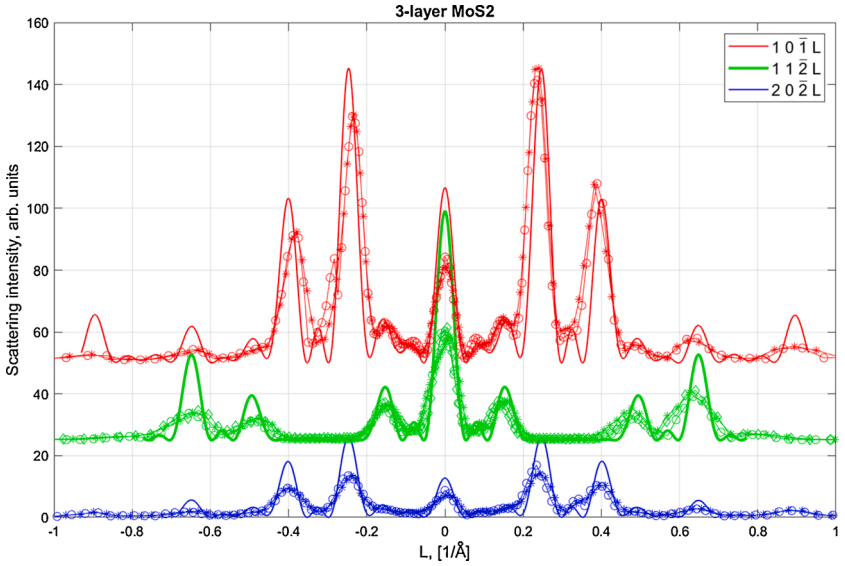

Fig. 8. Experimental (scatter plot) and simulated (solid line) scattering intensity distribution profiles along the 10 $\bar{1}$ L (red), 11 $\bar{2}$ L (green), and 20 $\bar{2}$ L (blue) relrods for a 3-layer MoS_2.

along the relrods for a bilayer MoS_2 is shown in Fig. 6. The experimental intensity distribution as well as the width of the peaks match the simulated data pretty well. Two neighbouring relrods of the *10* $\bar{1}$ type are plotted in red with circles and stars; the circles plot has a peak at L=-0.16 Å^{-1}, the star plot – at L=-0.16 Å^{-1}, matching the simulation. The asymmetry is seen in the *10* $\bar{1}$ *L* and *20* $\bar{2}$ *L* rods around $L = 0.16$ Å^{-1}, being the signature of the reduced symmetry of the crystal as described above.

One can see a slight disagreement in the peak's positions at higher L in the experimental data of the bilayer, most pronounced in *11* $\bar{2}$ *L* rods (green plots in Fig. 6). These may be attributed to a slightly different atomic arrangement in a bilayer compared to the bulk structure. The detailed analysis of the fine structure of the relrods goes beyond the scope of this paper.

One important structural parameter for a bilayer is the average distance between the layers. In order to evaluate the effect of the interlayer distance on the ED data, a bilayer model with an artificially increased distance between the layers by 1 Å (from 6.15 Å to 7.15 Å) was created. The intensity distributions along the relrods was then calculated and plotted together with those of the initial structure for comparison (Fig. 7). With the increase of the interlayer distance, the whole pattern shrinks and the peaks shift towards shorter L. The relative intensities of the peaks are modified, likely due to effectively shifted contributions of individual atomic scattering profiles.

The asymmetry of the *10* $\bar{1}$ *L* relrods for bilayer can lead to a special appearance of the normal incidence zone pattern, when recorded using a small Ewald sphere. This effect is analysed in Appendix C.

3.4.3. 3-, 4-, 5-layer MoS_2

The appearance of the relrods for a 3-layer MoS_2 is shown in Fig. 8. As mentioned above, the 3-layer structure has a horizontal mirror plane, the layer group is *p* $\bar{6}$ *m2*, the Laue class *6/mmm*. The symmetry of the relrods in respect to their base is clearly seen in Fig. 9.

Fig. 9 shows the relrods for a 4-layer crystal, the asymmetry of the

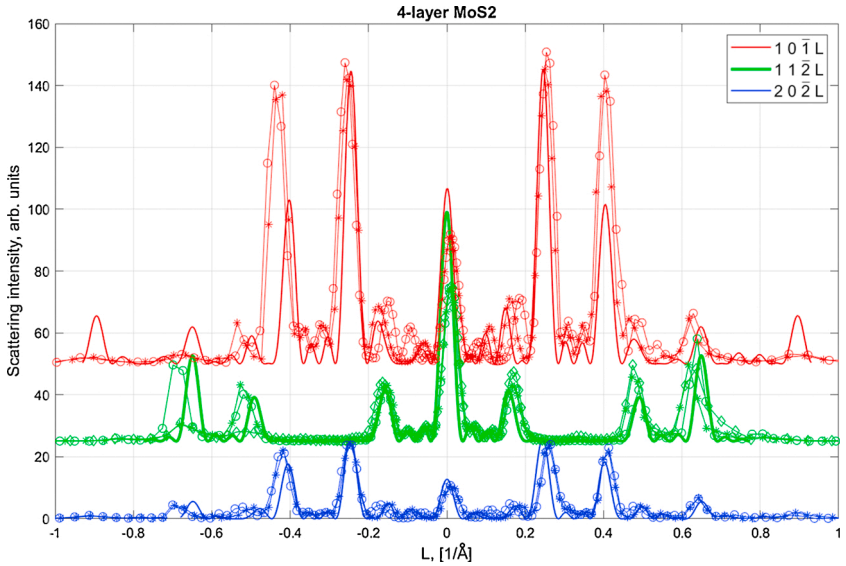

Fig. 9. Experimental (scatter plot) and simulated (solid line) scattering intensity distribution profiles along the 10 $\bar{1}$ L (red), 11 $\bar{2}$ L (green), and 20 $\bar{2}$ L (blue) relrods for a 4-layer MoS_2.

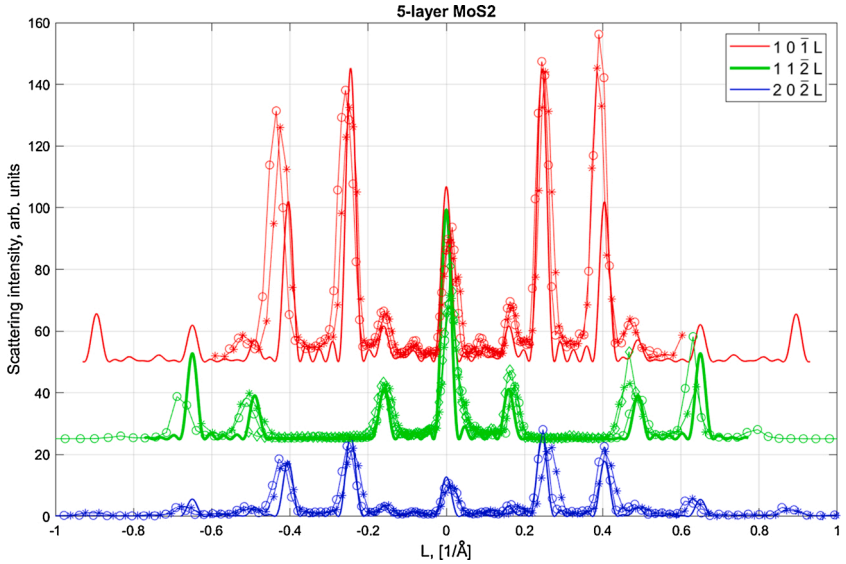

Fig. 10. Experimental (scatter plot) and simulated (solid line) scattering intensity distribution profiles along the 10 $\bar{1}$ L (red), 11 $\bar{2}$ L (green), and 20 $\bar{2}$ L (blue) relrods for a 5-layer MoS_2.

peaks in the range of 0−0.2 $Å^{-1}$ is evident. Fig. 10 shows the rods for a 5-layer crystal. The width of the peaks is comparable to that of the 4-layers crystal (Fig. 9), yet the appearance of the rods is different, matching the higher Laue class symmetry.

3.5. Determination of the number of layers

The analysis of the intensity profiles of the relrods clearly showed that with increase in layer number, the width of the peaks in the profiles decreases. The experimental width of the *10* $\bar{1}$ *L* relrod peak at $L = 0.22$ $Å^{-1}$, was measured for different crystals and plotted in Fig. 11 against the number of layers. This plot shows that the number of layers can unambiguously be determined from the relrod's characteristics – the effective width of the peaks in the intensity profiles and the layer group symmetry (reflected in the symmetry of the intensity distributions in respect to the base).

In this study the crystals were pre-selected based on their optical contrast. Two crystals were assigned to as consisting of 4-layers. The relrods of the first of these crystals are shown in Fig. 9. The second crystal showed, however, a completely different pattern (Fig. 10). From the analysis of the symmetry we could clearly assigned the last crystal to a 5-layer crystal.

In this study we collected large tilt series of diffraction patterns within the total goniometer tilt range of ±60°. Our analysis showed however that the most pronounced differences in the character of the relrods are concentrated around *L* below 0.2 $Å^{-1}$. In fact, it would be sufficient to sample the *10* $\bar{1}$ *L* relrod in the range ±0.16 $Å^{-1}$. The horizontal coordinate of the base of the *10* $\bar{1}$ *L* relrod $g_x = 0.37$ $Å^{-1}$, thus, a tilt range of ±30° should cover the targeted *L* range.

4. Conclusions

In this study 3D ED data of 2D hexagonal MoS_2 crystals of different thickness were investigated. Depending on the number of layers, the

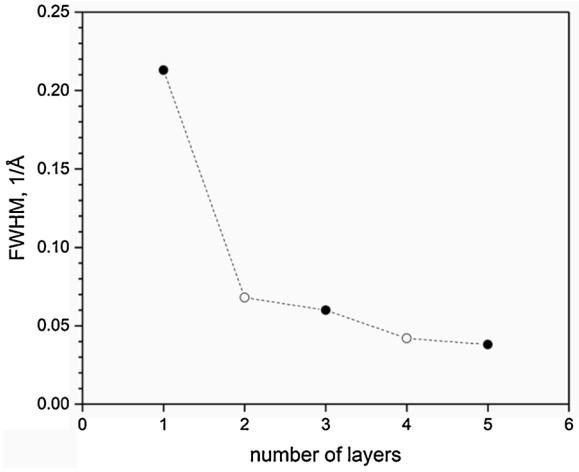

Fig. 11. Experimental peak's width in the intensity distribution of the relrods for MoS_2 crystals with different number of layers. Crystals with the p $\bar{6}$ m2 layer group, the Laue class 6/mmm are marked by black circles, crystals with the reduced symmetry p $\bar{3}$ m1, the Laue class $\bar{3}$ m1.

thin crystals have a different layer group symmetry: 2D MoS_2 crystals with an odd number of layers belong to the layer group *p* $\bar{6}$ *m2*, whereas crystals with an even number of layers have a lower symmetry of *p* $\bar{3}$ *m1* layer group. The difference in the symmetry is clearly reflected in the appearance of the reciprocal space: crystals with an even number of layers show asymmetric distribution of the intensities along the relrods. The symmetry of the reciprocal space combined with the width of the peaks along the relrods is an unambiguous measure for the number of layers in a crystal. This was demonstrated for 2D MoS_2 crystal with the number of layers 1, 2, 3, 4 and 5.

It must be underlined, that in this study we did aim at a qualitative analysis of the intensities' plots. Fine discrepancies between the simulated and experimental data are evident. These can be attributed to the *structural aspects* – the slight differences of the actual structure of few-layers MoS_2 compared to that of the bulk materials, to the *multiple scattering*, evidently present in the experimental data, as well as to the *instrumental transfer function* in the diffraction space, which has not been seriously addressed so far.

Funding

This work was supported by the German Science Foundation (DFG), project CRC 1279. We gratefully acknowledge the European Union funding in the frame of the Graphene Flagship.

Declaration of Competing Interest

No conflict of interest is to declare.

Acknowledgements

The authors would like to thank Martin U. Schmidt (Goethe University, Frankfurt am Main, Germany) and Bernd Souvignier (Radboud University Nijmegen, Netherlands) for fruitful discussions on layer groups and notation.

This work was supported by the German science foundation (DFG), research project CRC 1279. We gratefully acknowledge the European Union funding in the frame of the Graphene Flagship.

Appendix A. Optical contrast measurements

Fig. A1a shows an optical image of different MoS_2 crystals. The identified crystals are labelled by the number of layers (monolayer to 4-layer: 1 L–4 L). An exemplary colour image and corresponding grayscale images of the Red, Green, and Blue channels of a 3-layer (3 L) flake is shown as inset in (a). The contrast difference between the 2D nanosheet and the substrate is obtained by brightness profiles, the corresponding areas are highlighted by dashed rectangle in the insets and plotted in (b). Different colours in (b) mark the channel used. The order of magnitude of all measured contrast values is in very good agreement with the values published by Hai Li et al. (2013). This allowed us to precisely identify the crystal thicknesses, before transferring the MoS_2 crystals onto the TEM grid. Note that the flake labelled by 4 L* was later assigned to as a 5-layer crystal.

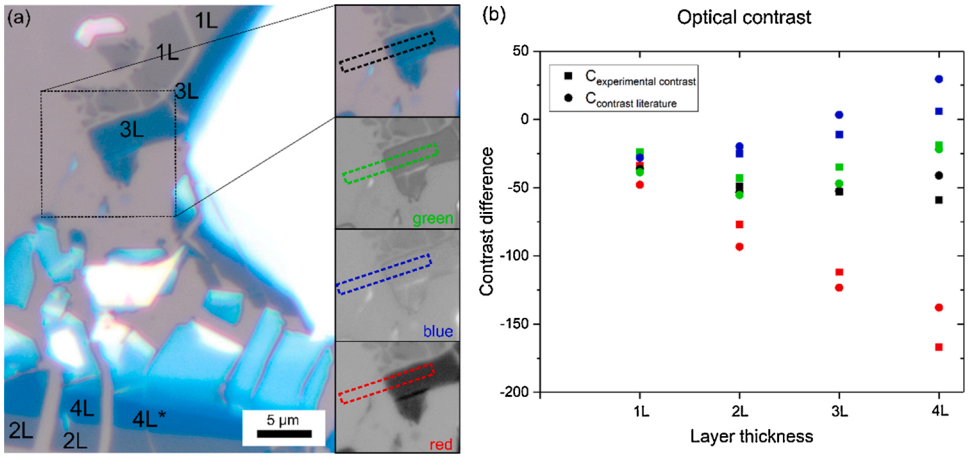

Fig. A1. (a) optical microscope image of MoS_2 crystals on a Si/SiO_2 90 nm substrate. An exemplary colour image of an 3 L flake and the corresponding grayscale images of the green, blue, and red channels are presented as insets. Dashed rectangle marks the area for contrast measurements. Contrast values of the marked sample regions (1 L – 4 L) in (a) are shown in (b). The experimental data points are presented as squares, the values published by Hai Li et al. (2013) as circles. The colours indicate the used channel of the camera; the black squares and circles represent the contrast difference of the raw colour image shown in (a).

Appendix B. Digital Micrograph tilt series acquisition script

```
result("\n************************************")
number a, a0, x, x0, y, y0, i, j, nx, ny, step, N;
RealImage img;
Object camera, acq_params;
String s, thispath;
result("\Current stage position\n");
a=round(EMGetStageAlpha());
a0=round(a);
x0=EMGetStageX();
x=x0;
y0=EMGetStageY();
y=y0;
step=1; // input goniometer tilt step here
N=20; // tilt interval in number of tilting steps
result("x=" + x0 + "\n")
result("y=" + y0 + "\n")
result("alpha=" + a0 + "\n")
//find the current camera
camera=CM_GetCurrentCamera();
acq_params=CM_GetCameraAcquisitionParameterSet(camera,  "Imaging",  "Acquire",
"Record", 0);
CM_CCD_GetSize(camera, nx, ny);
result("************************************\n")
for (i=1; i<N; i++)
{
 result("Frame number: " + i + ", tilt position: " + a + "\n");
   if ( ShiftDown() && ControlDown() )
   {
     OKDialog( "Script aborted by user" )
     Exit(0)
   }
   s="tilt_1_" + a;
   thispath="Z:\\DATA\\" + s ;
   img:=RealImage(s, 4, nx, ny)
   ShowImage(img);
   CM_AcquireImage(camera, acq_params, img);
   UpdateImage(img);
   a=a0+i*step;
   EMSetStageAlpha(a);
   result(thispath + "\n")
   saveasgatan3(img, thispath, 1);
 }
  result("current alpha " + a + "\n");
result("************************************")
```

Appendix C. Appearance of the normal incidence zone pattern of a bilayer

The slight asymmetry of the central peak in the $10\,\bar{1}\,L$ rod of the bilayer raises the question whether this effect can experimentally be observed within the normal incidence zone directly and used for the bilayer identification. Low energy electrons create a smaller Ewald sphere, which cuts relrods at higher positions L, further away from the relrod base (Fig. C1). The height at which the Ewald sphere cuts the relrod g_z, depends on the horizontal coordinate of the relrod base g_x, and the radius of the Ewald sphere, inversely related to the electron wavelength λ. Trivial geometrical considerations give the relation:

$$g_z = \frac{1}{\lambda} - \sqrt{\frac{1}{\lambda^2} - g_x^2} \quad (1)$$

For a bilayer, in accordance to the Laue class $\bar{3}\,m1$, the intensity distribution along the opposite relrods are related by an inversion centre at the origin of the reciprocal space. We define the asymmetry factor as the ratio of a relrod intensities at *L* and *-L*, which, for given symmetry, is equivalent to the intensity ratio of the opposite relrods at the same height *L*. For a symmetric relrod the asymmetry factor is equal to 1.

The blue plot in the Fig. C2a shows the relation between the acceleration voltage and the height of the relrod cut g_z, calculated using (1), for the *10* $\bar{1}$ *L* relrods of bilayer MoS_2. The lateral base position (see Fig. C1) of the *10* $\bar{1}$ *L* relrod g_x, corresponding to 10 $\bar{1}$ 0 reflection of the bulk structure, is 0.3666 $Å^{-1}$. The red plot (Fig. C2) represents the asymmetry factor for different g_z values.

At 300 kV used for the experiments, for *10* $\bar{1}$ *L* rod the g_z is about 0.001 $Å^{-1}$ (Fig. C2, vertical blue arrow originating at 300 kV), the asymmetry factor for this value is about 1% (horizontal red arrow in Fig. C2). At 10 kV the g_z height is about 0.008 $Å^{-1}$, corresponding to the asymmetry factor of about 6%, at 5 kV the asymmetry factor of 9% can be reached. This means that if the normal incidence zone of bilayer MoS_2 is recorded at 5 kV, the opposite reflections in the 10 $\bar{1}$ group (as defined in Fig. 2) should systematically show 9% difference in the intensities. We must however note that for the calculations we used a perfect geometry of bilayer, corrugation may additionally diminish the effective asymmetry factor.

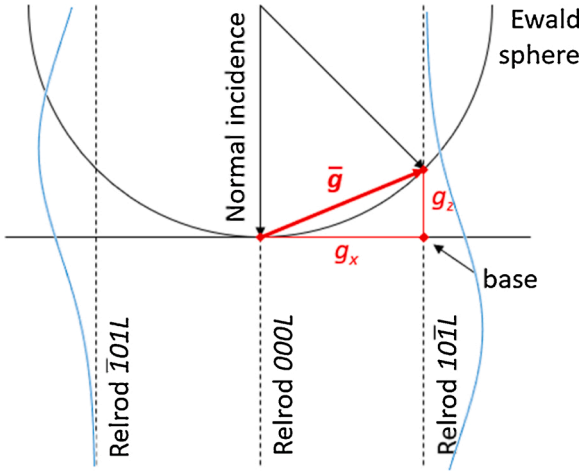

Fig. C1. A schematic representation of 3D ED geometry for 2D crystals: the normal incidence beam is orthogonal to the crystal surface, relrods are running along the normal incidence direction. Ewald sphere with a finite radius cuts a relrod at a certain height g_z, away from the rod base at L = 0. Asymmetric intensity distribution within the opposite relrods are schematically shown by the blue profiles.

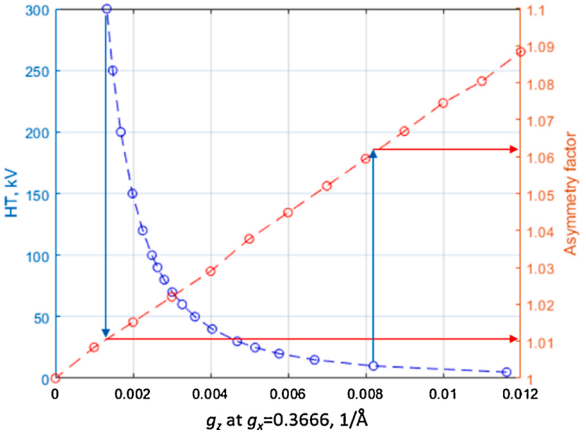

Fig. C2. Bilayer MoS_2: the relation between the electron acceleration voltage in kV and the height of the cut of the first relrod at $g_x = 0.3666$ $Å^{-1}$ (blue plot) calculated using (1) and the asymmetry factor for the 10 $\bar{1}$ L relrods (red plot) as defined in the text.

References

Brivio, J., Alexander, D.T.L., Kis, A., 2011. Ripples and layers in ultrathin MoS2 membranes. Nano Lett. 11, 5148–5153. https://doi.org/10.1021/nl2022288.

Choi, W., Choudhary, N., Hee Han, G., Park, J., Akinwande, D., Hee Lee, Y., 2017. Recent development of two-dimensional transition metal dichalcogenides and their applications. Mater. Today 20 (3), 116–130. https://doi.org/10.1016/j.mattod.2016.10.002.

Cromer, D.T., Liberman, D., 1970. Relativistic calculation of anomalous scattering factors for X rays. J. Chem. Phys. 53, 1891. https://doi.org/10.1063/1.1674266.

Das, S., Robinson, J.A., Dubey, M., Terrones, H., Terrones, M., 2015. Beyond graphene: progress in novel two-dimensional materials and van der Waals solids. Annu. Rev. Mater. Res. 45, 1–27. https://doi.org/10.1146/annurev-matsci-070214-021034.

Deb, P., Cao, M.C., Han, Y., Holtz, M.E., Xie, S., Park, J., Hovden, R., Muller, D.A., 2020. Imaging polarity in two dimensional materials by breaking Friedel's law. Ultramicroscopy 215, 113019. https://doi.org/10.1016/j.ultramic.2020.113019.

Dickinson, R.G., Pauling, L., 1923. The crystal structure of Molybdenite. JACS 45, 1466–1471. https://doi.org/10.1021/ja01659a020.

Gemmi, M., Mugnaioli, E., Gorelik, T.E., Kolb, U., Palatinus, L., Boullay, P., Hovmöller, S., Abrahams, J.P., 2019. 3D electron diffraction: the nanocrystallography revolution. ACS Cent. Sci. 5 (8), 1315–1329. https://doi.org/10.1021/acscentsci.9b00394.

Gogotsi, Y., Anasori, B., 2019. The rise of MXenes. ACS Nano 13 (8), 8491–8494. https://doi.org/10.1021/acsnano.9b06394.

Gorelik, T.E., Neder, R., Terban, M.W., Lee, Z., Mu, X., Jung, C., Jacob, T., Kaiser, U., 2019. Towards quantitative treatment of electron pair distribution function. Acta Cryst. B75, 532–549. https://doi.org/10.1107/S205252061900670X.

Kirilenko, D.A., Dideykin, A.T., Van Tendeloo, G., 2011. Measuring the corrugation amplitude of suspended and supported graphene. Phys. Rev. B 84, 235417. https://doi.org/10.1103/PhysRevB.84.235417.

Kopský, V., Litvin, D.B., 2002. International Tables for Crystallography Volume E: Subperiodic Groups. Springer nature. https://doi.org/10.1107/9780955360.

Lehnert, T., Lehtinen, O., Algara–Siller, G., Kaiser, U., 2017. Electron radiation damage mechanisms in 2D $MoSe_2$. APL 110, 033106. https://doi.org/10.1063/1.4973809.

Li, H., Wu, J., Huang, X., Lu, G., Yang, J., Lu, X., Xiong, Q., Zhang, H., 2013. Rapid and reliable thickness identification of two-dimensional nanosheets using optical microscopy. ACS Nano 7 (11), 10344–10353. https://doi.org/10.1021/nn4047474.

Liu, H., Neal, A.T., Zhu, Z., Luo, Z., Xu, X., Tomanek, D., Ye, P.D., 2014. Phosphorene: an unexplored 2D semiconductor with a high hole mobility. ACS Nano 8, 4033–4041. https://doi.org/10.1021/nn501226z.

Lv, R., Robinson, J.A., Schaak, R.E., Sun, D., Sun, Y., Mallouk, T.E., Terrones, M., 2015. Transition metal dichalcogenides and beyond: synthesis, properties, and applications of single- and few-layer nanosheets. Acc. Chem. Res. 48, 56–64. https://doi.org/10.1021/ar5002846.

Mak, K.F., Lee, C., Hone, J., Shan, J., Heinz, T.F., 2010. Atomically thin MoS_2: a new direct-gap semiconductor. PRL 105, 136805. https://doi.org/10.1103/PhysRevLett.105.136805.

Meyer, J.C., Geim, A.K., Katsnelson, M.I., Novoselov, K.S., Obergfell, D., Roth, S., Girit, C., Zettl, A., 2007a. On the roughness of single- and bi-layer graphene membranes. Solid State Commun. 143, 101–109. https://doi.org/10.1016/j.ssc.2007.02.047.

Meyer, J.C., Geim, A.K., Katsnelson, M.I., Novoselov, K.S., Booth, T.J., Roth, S., 2007b. The structure of suspended graphene sheets. Nature Lett. 446, 60–63. https://doi.org/10.1038/nature05545.

Nerl, H.C., Trøstrup Winther, K., Hage, F.S., Sommer Thygesen, K., Houben, L., Backes, C., Coleman, J.N., Ramasse, Q.M., Nicolosi, V., 2017. Probing the local nature of excitons and plasmons in few-layer MoS_2. NPJ 2d Mater. Appl. 1, 2. https://doi.org/10.1038/s41699-017-0003-9.

Novoselov, K.S., Geim, A.K., Morozov, S.V., Jiang, D., Zhang, Y., Dubonos, S.V., Grigorieva, I.V., Firsov, A.A., 2004. Electric field effect in atomically thin carbon films. Science 306, 666–669. https://doi.org/10.1126/science.1102896.

Pettersen, E.F., Goddard, T.D., Huang, C.C., Couch, G.S., Greenblatt, D.M., Meng, E.C., Ferrin, T.E., 2004. UCSF Chimera - a visualization system for exploratory research and analysis. J. Comput. Chem. 25 https://doi.org/10.1002/jcc.20084.

Song, l., Ci, L., Lu, H., Sorokin, P.B., Jin, C., Ni, J., Kvashnin, A.G., Kvashnin, D.G., Lou, J., Yakobson, B.I., Ajayan, P.M., 2010. Large scale growth and characterization of atomic hexagonal boron nitride layers. Nano Lett. 10, 3209–3215. https://doi.org/10.1021/nl1022139.

Sung, S.H., Schnitzer, N., Brown, L., Park, J., Hovden, R., 2019. Stacking, strain, and twist in 2D materials quantified by 3D electron diffraction. Phys. Rew Mat. 3, 064003 https://doi.org/10.1103/PhysRevMaterials.3.064003.

Ugeda, M.M., Bradley, A.J., Shi, S.-F., da Jornada, F.H., Zhang, Y., Qiu, D.Y., Ruan, W., Mo, S.-K., Hussain, Z., Shen, Z.-X., Wang, F., Louie, S.G., Crommie, M.F., 2014. Giant bandgap renormalization and excitonic effects in a monolayer transition metal dichalcogenide semiconductor. Nat. Mater. 13, 1091–1095. https://doi.org/10.1038/NMAT4061.

Wang, H., Yuan, H., Hong, S.S., Li, Y., Cui, Y., 2015. Physical and chemical tuning of two-dimensional transition metal dichalcogenides. Chem. Soc. Rev. 44, 2664–2680. https://doi.org/10.1039/c4cs00287c.

Xia, F., Wang, H., Xiao, D., Dubey, M., Ramasubramaniam, A., 2014. Two-dimensional material nanophotonics. Nat. Photonics 8, 899–907. https://doi.org/10.1038/NPHOTON.2010.271.

Xu, M., Liang, T., Shi, M., Chen, H., 2013. Graphene-like two-dimensional materials. Chem. Rev. 113, 3766–3798. https://doi.org/10.1021/cr300263a.

Yin, X., Ye, Z., Chenet, D.A., Ye, Y., O'Brien, K., Hone, J.C., Zhang, X., 2014. Edge nonlinear optics on a MoS_2 atomic monolayer. Science 344, 488–490. https://doi.org/10.1126/science.1250564.

Zavabeti, A., Jannat, A., Zhong, L., Haidry, A.A., Yao, Z., Ou, J.Z., 2020. Two-dimensional materials in Large-Areas: synthesis, properties and applications. Nano-Micro Lett. 12, 66. https://doi.org/10.1007/s40820-020-0402-x.